Contents lists available at SciVerse ScienceDirect

CIRP Annals Manufacturing Technology

Journal homepage: www.elsevier.com/locate/cirp

Effect of recycled swarf and spherical Ti-6Al-4V feedstocks on laser directed energy deposition additive manufacturing

Sarah Wolff[a], Marwan Haddad[a], Jianyue Zhang[b], Alan Luo[b]

[a] *Department of Mechanical and Aerospace Engineering, The Ohio State University, Columbus, OH, 43210, USA*
[b] *Department of Materials Science and Engineering, The Ohio State University, Columbus, OH, 43210 USA*

Submitted by Frank Pfefferkorn (1), Madison, WI 53706 USA

Feedstock from locally-sourced, recycled Ti-6Al-4V (Ti64) swarf is a low-cost alternative to atomized powder and encourages circular additive manufacturing. This study investigates the feasibility of Ti64 swarf as feedstock for laser directed energy deposition (L-DED) additive manufacturing. Ti64 swarf was recycled and ball-milled into irregular-shaped powder and compared to spherical plasma-atomized powder in powder flow, melt flow, and resulting microstructure. *In situ* monitoring showed that plasma-atomized powder had laminar flow during deposition and that ball-milled swarf powder had turbulent flow. Plasma-atomized powder had steady melt pool dynamics and acicular microstructure. Ball-milled swarf powder caused melt pool fluctuation and equiaxed microstructure.

Additive manufacturing, Powder, *In situ* monitoring

1. Introduction

Ti-6Al-4V (Ti64) is a titanium alloy with a high strength-to-weight ratio used widely for transportation, aerospace, and biomedical applications. Additive manufacturing (AM) of Ti64 components has increased in demand recently due to design flexibility, geometric complexity, and feedstock material savings compared to conventional processing that entails multiple steps of joining and subtractive manufacturing. However, many metal AM processes require plasma or gas-atomized powder feedstock that are costly and energy intensive [1]. A feedstock alternative is Ti64 swarf, or discarded material from industrial scale production of Ti64 fabrication. Due to the high cost of Ti64 fabrication, recycling Ti64 has gained attention, with Ti64 swarf, or scrap, as a major source for high-efficiency recycling [2]. Therefore, this study explores Ti64 swarf as a feedstock material for metal AM processes such as Laser Directed Energy Deposition (L-DED), a possible application of industrial symbiosis [3, 4].

L-DED is an AM process that deposits powder feedstock into a melt pool created by a laser source to manufacture a part by subsequent printed layers [5]. Previous work investigated the feasibility of recycling metal swarf for L-DED processes. For example, Mahmood *et al.* showed the feasibility of reducing material usage by printing with carbon steel chips [5]. Fullenwider *et al.* recycled 304 L stainless steel machining chips into feedstock powder and successfully printed single layer tracks with L-DED, resulting in melt tracks with similar morphology to those printed with gas-atomized powder [6]. Jackson *et al*. compared 316L parts from L-DED gas-atomized powder and those from mechanically generated feedstock, finding that their microstructure, surface texture, and most mechanical properties were similar, with an increase in tensile strength for parts from mechanically generated feedstock [7]. Murray *et al.* found that chips that were not cleaned from cutting fluid residue were viable feedstock for the L-DED process [8].

Relative to the literature, the novelty of the presented work is in (Fig. 1): (1) *In situ* and *ex situ* comparison analysis, before, during, and after printing, between plasma-atomized (PA) Ti64 powder and ball-milled (BM) Ti64 swarf powder and (2) L-DED printing of PA Ti64 powder and BM Ti64 swarf to compare results from both powder feedstocks. Overall, the findings show the viability of recycled Ti64 swarf powder as an alternative feedstock for L-DED processes. Captured *in situ* high-speed images suggest that process dynamics differ between the different powder and their outcomes.

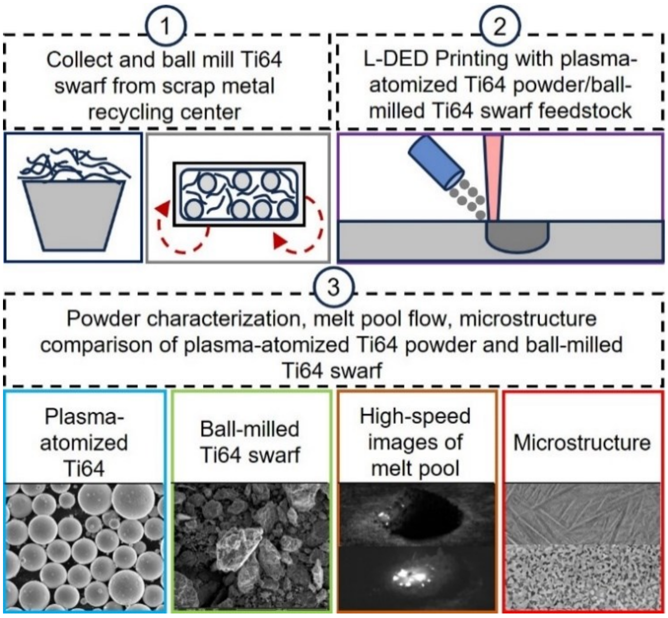

Figure 1. Comparison study between plasma-atomized (PA) powder and ball-milled (BM) Ti64 swarf powder using *in situ* and *ex situ* analysis.

2. Material and methods

This study concerns two types of feedstocks for the L-DED process: PA Ti64 powder and recycled, BM Ti64 swarf powder. The Ti64 PA powder was from AP&C Powder Metallurgy (GE Additive - Canada) with a size distribution between 45-106 µm. The Ti64 swarf (Fig. 2) was collected from a local metal scrap recycling facility (Stargate Metals - Columbus, OH, USA), ranging in size from 5 to 25 mm in width. The swarf represented material from cutting operations, as observed by the swarf morphology in Fig. 2. Most of the swarf were segmented machining chips, or serrated, with 6s and 9s shapes with a smooth side and a serrated side (see Supplementary Material). The swarf was then BM for 6 hours with 10 mm diameters stainless steel balls at 600 rpm. There was no cleaning before or after ball milling because most impurities from machining coolant evaporates during the L-DED process [8]. Subsequently, a vibratory sieve shake sieved the powder with 100 and 325 meshes for 2 hours to achieve a particle size distribution between 43 and 150 µm for optimal L-DED deposition [9]. Finally, the BM powder was in a vacuum drying oven at 423 K for 24 hours to remove moisture.

The printing occurred in an in-house custom L-DED glovebox system with a 3-axis motorized stage, consisting of a single nozzle with a hopper (20 mL) designed for small quantity testing and an ytterbium fiber laser head with a 400 W maximum power. During printing, the laser diameter was 2 mm and offset above the focal plane by 30 mm. An off-axis high speed camera (FASTCAM SA-Z-Photron Japan) captured real-time images from outside the glovebox. Energy Dispersive X-Ray Analysis (EDX) measured the powder composition. X-ray diffraction (XRD) analysis detected the phases in the powder. Lastly, Optical Microscope (OM) and Apreo I (FEI Apreo LoVac Analytical) high resolution scanning electrical microscope (SEM) revealed the final parts' microstructures.

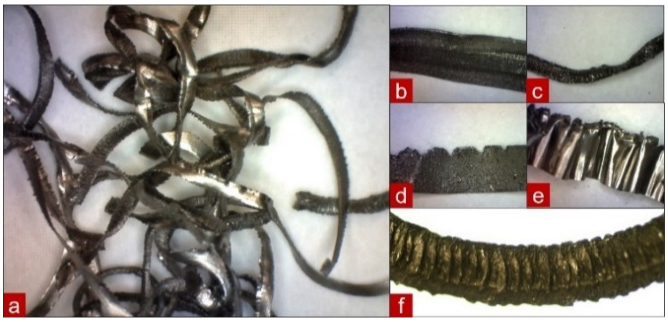

Figure 2. a) Representative batch of Ti64 swarf, or machining chips. The different types of chips include b) continuous, c) wavy, d) elemental, e) discontinuous, and f) segmented.

3. Results and discussion

3.1. Powder characteristics

Figures 3a and b are SEM images of PA and BM powder. BM powder particles (Fig. 3b) have irregular shapes and sizes compared to the spherical shapes of the PA powder particles (Fig. 3a). In addition, BM powder included small irregular shaped particles with a smaller size distribution than that of PA powder. The distributions of the effective diameter (see supplementary materials) for both powder types are in the boxplots in Fig. 3c. The BM powder particles have a lower average effective diameter (around 40 µm) than that of the PA powder (around 55 µm), and a lower first quartile (around 29 µm for BM powder and 50 µm for PA powder). Although the average effective diameter size of the BM powder is close to the 325-mesh opening size (43 µm), a sizable portion (25 %) of BM powder is smaller than 29 µm, compared with PA powder, where most of the effective diameters are above 50 µm.

Meanwhile, multiple EDX measurements of BM powder do not show impurities such oxygen or residue from machining lubricants. XRD scans displayed in Fig. 3d show that the peak patterns for both materials match approximately and align with (hkl) values of the Ti Hexagonal Close-Packed (HCP) α phase [10]. However, BM powder's XRD patterns exhibit a slight difference in peak intensity and width with a shift to the left, which can be correlated to the crystallite size and presence of micro-strains from the ball milling process [11, 12].

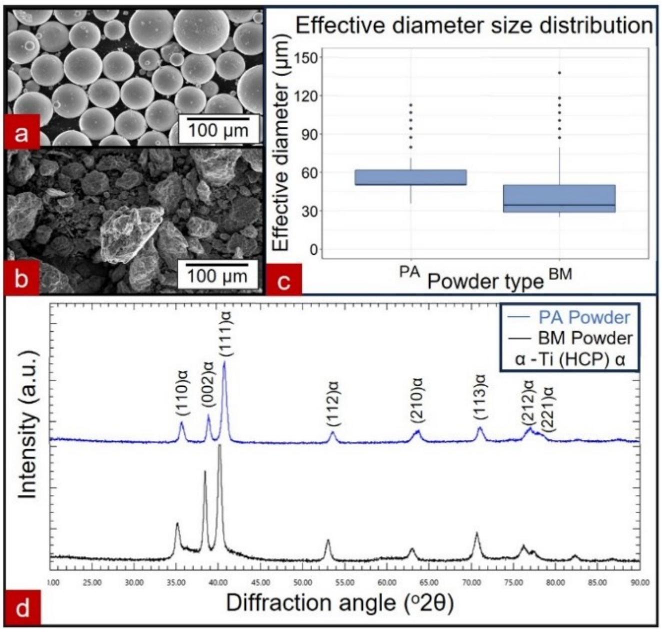

Figure 3. a) and b) SEM images of PA and BM powder, c) box plots of the effective diameter size distribution for PA and BM powder, d) XRD patterns of PA and BM powder.

3.2. Powder flow

To clearly see the powder flow during printing, the laser was OFF, and the argon carrier gas had a pressure of 34.5 kPa. The mass flow rates for BM and PA powder were 15.10^{-3} g/s and 42.10^{-3} g/s, respectively. The difference in flow rates is due to both the irregular shape of the BA powder and greater distribution of very small particles in the BA (<30 µm), even after sieving. High-speed images were captured at 10,000 fps with a field of view (FOV) of 15 mm x 15 mm (1024 x 1024 pixels) and a pixel size of 20 µm.

The images show the trajectory of the powder particles deposited from the nozzle until impact with the Ti64 substrate. Rendered recordings of the high-speed images are in Supplementary Videos S1 and S2. For PA powder in Supplementary Video S1, the argon gas flow was laminar, and the kinetic energy of the powder particles did not decrease after impact with the substrate as the speed before and after impact was around 3.3 m/s. Figure 4a displays the traced trajectory of a PA powder particle characterized by a straight line.

As for the BM powder flow in Supplementary Video S2 and Fig. 4b, the flow is laminar when particles exit the nozzle, and then transitions (white horizontal dashed line) to turbulent flow before impact with the underlying Ti64 substrate. Furthermore, the traced trajectory of the BM powder particle (yellow arrow lines) diverges away from the trajectory of the center axis of the nozzle (red dashed line), opposed to the straight-line trajectory of the traced PA powder particle in Fig. 4a. Moreover, a turbulent vortex materializes behind the BM powder stream after impact with the substrate surface. Moreover, there is loss of kinetic energy as the measured speed before and after impact was around 3.4 m/s and 0.8 m/s, respectively. Figure 4.b shows the traced trajectory of an irregular BM powder particle, the laminar gas flow near the nozzle, the turbulent flow above the substrate, and the vortex behind the flow. In addition, the BM powder flow is denser than the PA powder flow even though the mass flow rate of BM powder is smaller. The occurrence of the turbulent flow, the vortex, and the dense flow is because of the irregular shape of the BM powder and the existence of a significant amount of small powder particles in the BM powder interacting with the argon gas flow.

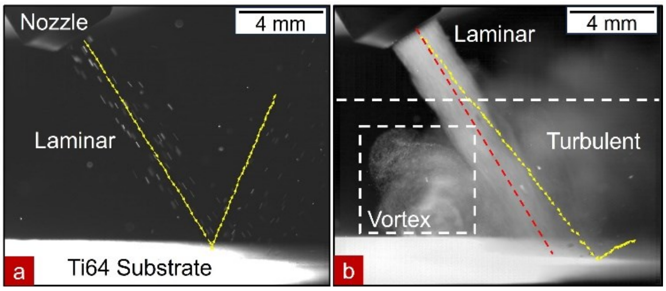

Figure 4. Powder flow of a) PA and b) BM powder colliding with the Ti64 substrate without turning the laser ON.

3.3. Printing with L-DED

L-DED printing for both powder feedstocks occurred in an inert environment (<100 ppm oxygen concentration). The printing parameters for both powders were 276 W laser powder and 4 mm/s scanning speed. High-speed images were captured at 10,000 fps with a FOV of 14 x 14 mm (1024 x 1024 pixels) and 20 µm/pixel resolution. Supplementary Videos S3 and S4 show the printing, or laser melting, of a single layer of 3mm length with PA powder and BM powder on a Ti64 substrate. The videos show the onset of melting, a molten pool in steady-state, and solidification at the end of a print. The supplementary videos show how both deposited layers for PA and BM powder are continuous, without balling, and similar in geometry to each other. However, powder particles from the PA and BM feedstock interact differently with the melt pool.

In Supplementary Video S3, the molten pool is steady during printing. A portion of the PA powder floats on the top of the surface of the molten melt pool for an interval of time before submerging into the liquid metal. This phenomenon was also recorded in a previous work by Haley *et al.* on L-DED with 316L spherical gas atomized feedstock [13]. Additionally, bright spots (largest measured area 0.1 mm^2) emerged on the surface of the molten metal as surface pores, which can increase in size, coalesce, explode, or solidify resulting in a rough surface of the track as reported by Zhang *et al.* [14]. Figure 5a is an example of a captured image during printing PA powder. Floating powder particles are located on the top of the surface of the melt pool, while bright white spots are at the liquid-solid boundary or in the center of the melt pool. Fig 5b is a representation of the L-DED process when Ti64 PA powder is the deposited feedstock, with floating powder particles on the surface of the melt pool and the formation of bright spots on the molten metal surface.

In Supplementary Video S4, during the deposition of BM powder, the surface of the melt pool fluctuates at a rate faster than the 0.1 ms time interval between frames, with apparent surface ripples. Contrary to PA powder, BM powder particles do not float on top of the molten surface. However, large bright white spots (largest measured area 0.15 mm^2) are on the melt pool surface, which lead to large pores and a rough solidified surface.

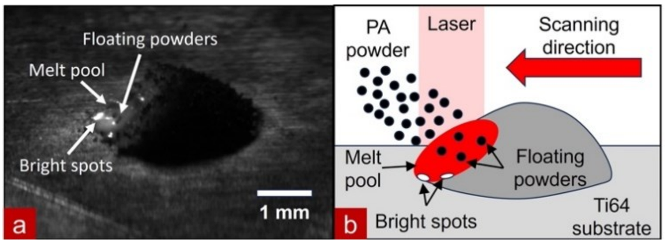

Figure 5. a) Floating PA powder particles and bright spots on the surface of the melt pool. b) Schematic of PA powder deposition with L-DED.

Figure 6 illustrates the fluctuation and rippling of the melt pool surface and the non-presence of floating particles for BM powder deposition. At the start of the image sequence (Fig. 6a), a BM powder particle collides with the surface of the melt pool, which induces splashing of the liquid metal and the formation of a bright spot on the melt pool surface. Then in Fig. 6b, after a time interval of 0.1 ms (one frame), the molten liquid engulfs the powder particles. Thus, the shape of the BM powder may be a factor in the interaction of BM powder particles with the argon carrier gas and the molten pool. This interaction causes splashes that subsume the powder particles into the molten pool, generating high frequency ripples on the surface. Another cause for fluctuations is the turbulent flow and vortex of the BM powder flow, discussed in the powder flow analysis section and observed above the melt pool in Supplementary Video S4, which induces vibration at the top surface of the molten metal. Figure 6c is a representation of the L-DED process when BM powder deposits into the melt pool, displaying the ripples and the formation of large bright spots when the irregular powder particle penetrates the melt pool surface.

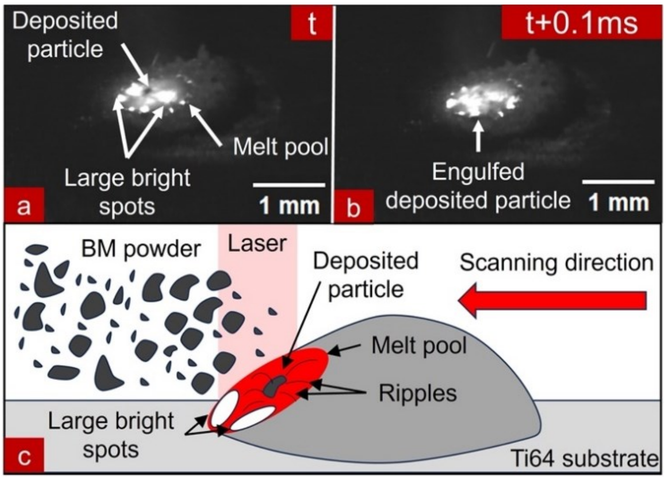

Figure 6. a) At time t, a BM powder particle impacts the surface of the melt pool, causing a splash in the molten metal and forming bright spots. b) At time t+ 0.1 ms, the fluctuating liquid metal engulfs the powder particle. c) Schematic of the deposition of BM powder with L-DED.

3.4. Microstructure

Two one-layer samples with a length of 10 mm were printed with the same input parameters and showcased the same melt pool phenomena as those used and observed in the previous section. After printing, the cross-sections of the two samples were polished and immersed in a Kroll's reagent solution. Using OM and SEM, the microstructures were analyzed.

For the sample printed with PA powder, there are no pores in the cross-section (Fig. 7a) and there is an acicular (needle-like) microstructure in Fig. 7b, indicating martensitic transformation caused by the rapid cooling rate of the melt pool [15]. The observed microstructure is consistent with the large mass flow rate of the PA powder into the melt pool, which causes a rapid cooling rate. A larger mass flow rates attenuates the laser beam and absorbs more laser energy away from the substrate, prompting a smaller melt pool (0.7 mm in length) and a rapid cooling rate.

Alternatively, the cross-section of the BM powder sample reveals pores with varying sizes (Fig. 7c) and an equiaxed fine grain microstructure (Fig. 7d). Factors for the formation of porosity and fine grain microstructure are the irregular shape and chemical composition of the BM powder, the interactions among the irregular powder particles, the molten pool, and the argon gas, the lower mass flow rate, along with the turbulent flow of the powder flow. First, the formation of pores is from the entrapment of argon gas by the irregular shape of the powder inside the melt pool . Because the swarf is not cleaned of machining coolant before the additive manufacturing process, an additional source of pores is the release of undetected impurities from coolant upon vaporization inside the melt pool.. Lastly, the existence of large pores is due to the pore coalescence mechanism of smaller pores into larger ones. Similar dynamics were observed for hydride–dihydride (HDH) irregular Ti64 powder in L-DED using X-ray high speed imaging by Wang *et al*. and Haddad *et al.* [16, 17]. Second, the smaller mass flow rate of the BM powder moderately attenuates the laser beam which leads to a bigger absorption of laser energy into the substrate. The additional heating creates a large melt pool (1 mm in length). With a larger melt pool, the cooling rate is slower during solidification, and the martensitic phase transformation is unachievable. Third, these interactions and powder flow induced fluctuations that may function as sources of high frequency vibration in the liquid metal. The high-intensity vibration of molten pool results in the formation of cavitation and consequent implosion of cavities. Therefore, the resulting intensive shock waves refine Ti64 grain nucleation and forms equiaxed grains in samples produced with BM powder. Ultrasonic vibration techniques in molten metal alloys lead to similar grain refinement mechanisms [18].

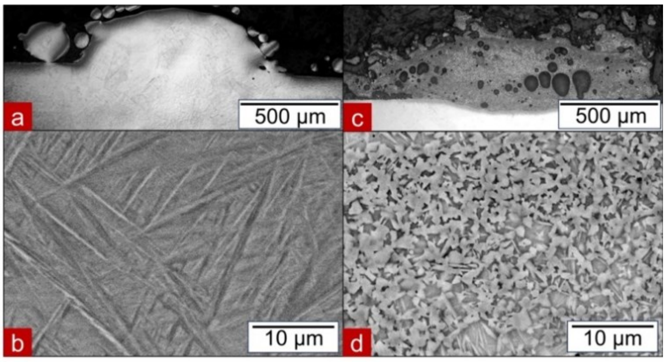

Figure 7. a) OM image of PA powder printed sample cross-section. b) SEM image of acicular microstructure in the PA powder printed sample. c) OM image of a BM powder printed sample cross-section. d) SEM image fine equiaxed grain microstructure of a BM powder printed sample.

4. Conclusions

In this work, recycled Ti64 swarf was ball milled into powder feedstock and compared with Ti64 plasma-atomized feedstock for L-DED process applications. *In situ* with *ex situ* analysis led to the following conclusions:

- Ball-milled (BM) powder from recycled Ti64 swarf had a turbulent powder flow stream during deposition, while plasma-atomized (PA) powder had a laminar flow stream.
- The turbulent flow from the BM powder flow stream interacted with the molten pool, triggering a high frequency fluctuation mechanism in the melt pool flow. In contrast, a steady state melt pool was observed during PA powder deposition.
- Printed samples with BM powder had an equiaxed fine microstructure due to the fluctuation mechanism of the molten pool. Printed samples with PA powder had an acicular microstructure.

Overall, this work shows the feasibility of recycled Ti64 swarf as feedstock for L-DED additive manufacturing, with the understanding that different microstructures result based on feedstock selection. Future work will focus on employing other *in situ* methods to further study the behavior of BM powder recycled from Ti64 swarf during the L-DED process.

Supplementary Materials

Please refer to the supplementary materials for details on Ti64 swarf and its characterization, calculation of powder effective diameters, and the four high-speed imaging videos.

Acknowledgement

National Science Foundation (NSF) grant CMMI-2245141 supported this work. The authors would like to thank CIRP Fellow Frank Pfefferkorn from the University of Wisconsin-Madison for discussions and his sponsorship. The authors would like to thank the following from The Ohio State University for experimental support: Aslan Bafam Alamdari, Sizhe Xu, Alex Thomas, Dylan Van Tassell, Daniel Veghte, Hendrik Colijn, Mason Darnell, Jerome Klein, Nathan Heniken, and Aeriel Murphy-Leonard.

References

[1] Yan, M., & Yu, P., 2015, An Overview of Densification, Microstructure and Mechanical Property of Additively Manufactured Ti-6Al-4V — Comparison among Selective Laser Melting, Electron Beam Melting, Laser Metal Deposition and Selective Laser Sintering, and with Conventional Powder, In: Sintering Techniques of Materials, InTech.

[2] Takeda, O., Okabe, T.H., 2019, Current Status of Titanium Recycling and Related Technologies, JOM,71:1981–1990.

[3] Kobayashi, H., Murata, H., Fukushige, S., 2020, Connected lifecycle systems: A new perspective on industrial symbiosis, Procedia CIRP, 90, 388-392.

[4] Horn, M., Prestel, L., Schmitt, M., Binder, M., Schlick, G., Seidel, C., Reinhart, G., 2020, Multi-Material additive manufacturing–recycling of binary metal powder mixtures by screening, Procedia CIRP, 93, 50-55.

[5] Mahmood, K., Khan, A., Pinkerton, A., 2011, Laser Metal Deposition of Steel Components using Machining Waste as Build Material, CLEO: 2011 - Laser Science to Photonic Applications.

[6] Fullenwider, B., Kiani, P., Schoenung, J.M., Ma, K., 2019, Two-stage ball milling of recycled machining chips to create an alternative feedstock powder for metal additive manufacturing, Powder Technol, 342:562-571.

[7] Jackson, M.A., Morrow, J.D., Thoma, D.J., Pfefferkorn, F. E., 2020, A comparison of 316 L stainless steel parts manufactured by directed energy deposition using gas-atomized and mechanically-generated feedstock, CIRP Annals, 69/1:165-168.

[8] Murray, J.W., Speidel, A., Jackson-Crisp, A., Smith, P.H., Constantin, H., Clare, A.T., 2021, Unprocessed machining chips as a practical feedstock in directed energy deposition, Int. J. Mach. Tools Manuf, 169.

[9] Singh, A., Kapil, S., Das, M., 2020, A comprehensive review of the methods and mechanisms for powder feedstock handling in directed energy deposition, Addit. Manuf, 35.

[10] Novoselova, T., Malinov, S., Sha, W., Zhecheva, A., 2004, High-temperature synchrotron X-ray diffraction study of phases in a gamma TiAl alloy, Mater. Sci. Eng. A: Structural Materials Properties Microstructure and Processing, 371:103-112.

[11] Khatirkar, R.K., Murty, B.S., 2010, Structural changes in iron powder during ball milling, Mater. Chem. Phys, 123/1:247-253.

[12] Lucks, I., Lamparter, P., Mittemeijer, E.J., 2004, An evaluation of methods of diffraction-line broadening analysis applied to ball-milled molybdenum. J. Appl. Cryst., 37:300-311.

[13] Haley, J.C., Schoenung, J.M., Lavernia, E.J., 2018, Observations of particle-melt pool impact events in directed energy deposition, Addit. Manuf, 22:368-374.

[14] Zhang, P., Zhou, X., Cheng, X., Sun, H., Ma, H., Li, Y., 2020, Elucidation of bubble evolution and defect formation in directed energy deposition based on direct observation, Addit. Manuf, 32.

[15] Akram, J., Pal, D., Stucker, B., 2019, Establishing Flow Stress and Elongation Relationships as a Function of Microstructural Features of Ti6Al4V Alloy Processed using SLM. Designs 3, 2:21.

[16] Wang, H., Gould, B., Haddad, M., Wu, Z., Wolff, S.J., 2022, In situ X-ray imaging of directed energy deposition of metals: The comparisons of delivery performance between spherical and irregular powders, J. Manuf. Process, 79:11-18.

[17] Haddad, M., Alamdari, A.B., Kankaria, K.V., Wang, H., Gould, B., Wolff, S.J., 2023, Gas bubble coalescence in laser directed energy deposition of irregular HDH titanium alloy powder feedstock, Manuf. Lett, 35/Supplement:665-676.

[18] Han, Q., 2015, Ultrasonic Processing of Materials, Metall. Mater. Trans. B, 46:1603–1614.